Current Opinion in Solid State and Materials Science 19 (2015) 190–199

Contents lists available at ScienceDirect

Current Opinion in Solid State and Materials Science

journal homepage: www.elsevier.com/locate/cossms

Mechanics of stretchable batteries and supercapacitors

Yihui Zhang [a,b,*], Yonggang Huang [a], John A. Rogers [c]

[a] Departments of Civil and Environmental Engineering and Mechanical Engineering, Center for Engineering and Health, Skin Disease Research Center, Northwestern University, Evanston, IL 60208, USA
[b] Center for Mechanics and Materials, Tsinghua University, Beijing 100084, China
[c] Department of Materials Science and Engineering, Frederick Seitz Materials Research Laboratory, University of Illinois at Urbana-Champaign, Urbana, IL 61801, USA

ARTICLE INFO

Article history:
Received 28 October 2014
Accepted 2 January 2015
Available online 16 January 2015

Keywords:
Energy storage
Mechanics
Electrodes
Wrinkling
Serpentine interconnects
Postbuckling
Batteries
Supercapacitors

ABSTRACT

The last decade has witnessed fast developments and substantial achievements that have been shaping the field of stretchable electronics. Due to a persistent need of equally stretchable power sources, especially for some emerging bio-integrated applications enabled by this unusual class of electronics, stretchable energy storage systems have been attracting increasing attentions in the past few years. This article reviews the mechanics of stretchable batteries and supercapacitors that are enabled by novel structural designs of hard and soft components, involving four representative strategies (i.e., wavy, wrinkled design, origami design, serpentine bridge-island design, and fractal inspired bridge-island design). The key mechanics of each strategy is summarized, with focuses on the design concepts, unique mechanical behaviors, and analytical/computational models that guide the design optimization. Finally, some perspectives are provided on the remaining challenges and opportunities for future research.

1. Introduction

The field of stretchable electronics has been evolving very rapidly during the last decade, from the perspective of developing fundamental enabling technologies, exploring applicable device systems, and opening up new application opportunities. This class of electronics could offer the functionalities of established technologies [1,2], while with superior mechanical attributes that are inaccessible to traditional electronics, e.g., stretched like a rubber band, twisted like a rope, and bent around a pencil tip, without mechanical fatigue or any significant change in operating characteristics. Those superior mechanical characteristics pave the way to a range of innovative and realistic applications that could not be addressed with any other approach, such as "epidermal" health/wellness monitors [3–5], eyeball-like digital cameras [6,7], soft surgical instruments [8–10], and sensitive robotic skins [11–13].

To enable conformal integration of stretchable electronic devices with human tissues, there is a persistent need for developing equally stretchable energy storage systems to complete the entire package. However, the stretchable energy storage systems did not receive much attention until 2009 [14], partially due to the relative complex constructions, or the requirement of sufficiently large energy density. Many important progresses have been achieved in recent years with the development of new design concepts and enabling technologies. In general, there are two routes to stretchable energy storage systems: (1) developing novel materials that are intrinsically stretchable to serve as key components (e.g., electrodes and electrolytes) of the batteries/supercapacitors [15–20]; (2) devising novel structural designs for heterogeneous integration of hard and soft components to result in device systems that are stretchable [14,21–31]. This paper will focus on the latter route, aiming to provide a review on the recent advances in the mechanics of stretchable batteries and supercapacitors.

Fig. 1 summarizes four representative strategies of structural designs that have been exploited to achieve stretchable batteries/supercapacitors: (i) wavy, wrinkled design [14,21–25] through use of prestrain in soft elastomeric substrate; (ii) origami design [26,27] by exploiting predefined crease patterns; (iii) serpentine bridge-island design [28,29], and (iv) fractal inspired (or self-similar) bridge-island design [30], with the aid of photolithography technology. The subsequent Sections 'Wavy, wrinkled design', 'Origami design', 'Serpentine bridge-island design', and 'Fractal inspired bridge-island design' will give an overview of the key mechanics in each of those strategies, including the design concepts, superior mechanical performances, and analytical/computational models that guide the design optimization. Section 6 presents a brief

* Corresponding author at: Departments of Civil and Environmental Engineering and Mechanical Engineering, Center for Engineering and Health, Skin Disease Research Center, Northwestern University, Evanston, IL 60208, USA.

E-mail address: yihui.zhang2011@gmail.com (Y. Zhang).

http://dx.doi.org/10.1016/j.cossms.2015.01.002
1359-0286/

discussion on the remaining challenges and opportunities for future research.

2. Wavy, wrinkled design

The wavy, wrinkled designs were exploited in several studies of stretchable supercapacitors and batteries to form stretchable electrodes made of single-walled carbon nanotube macrofilms [14,22], polypyrrole (PPy) [21], or graphenes [24,25]. The key of this strategy is to introduce an initial strain difference in the soft substrate (e.g., PDMS or ecoflex) and hard thin films (e.g., metal or semiconductor), either by thermally induced mismatch [32] or mechanical prestrain [33,34]. Fig. 2a presents schematically the fabrication procedure of wavy silicon ribbons that are fully bonded on an elastomeric substrate [34]. This strategy involves thin single-crystal Si ribbons or complete integrated devices (e.g., transistors, diodes) that are formed on a mother wafer by traditional lithographic processing, and a prestrained elastomeric substrate (PDMS). Etching of the top Si and SiO_2 layers of a SOI wafer could eliminate the bonding between the ribbon structures and the underlying wafer, such that contacting the prestrained PDMS to the ribbons leads to their transfer to the PDMS substrate. Releasing the prestrain in the PDMS substrate then leads to formation of highly periodic, stretchable wavy ribbon structures. During this procedure, UV/ozone activation of PDMS surface can be adopted to enable strong, covalent interfacial bonding between Si ribbons and PDMS substrate, because of silane coupling reactions between hydroxyl groups on the native oxide surfaces of Si ribbons [35]. Fig. 2b presents scanning electron micrographs (SEM) of wavy, single-crystal Si ribbons generated with the use of ~15% prestrain in the PDMS.

Many mechanics models have been developed to describe, in a quantitative manner, the formation of wavy ribbon structures, as well as their stretchability and compressibility, which have been summarized in two review papers [36,37]. As such, only the key results will be mentioned herein. In the regime of small prestrain (e.g., $0.5\% < \varepsilon_{pre} < 5\%$), an energy approach was developed [38,39] based on small-deformation theory to determine the buckling geometry, in which the linear, elastic substrate is modeled as a

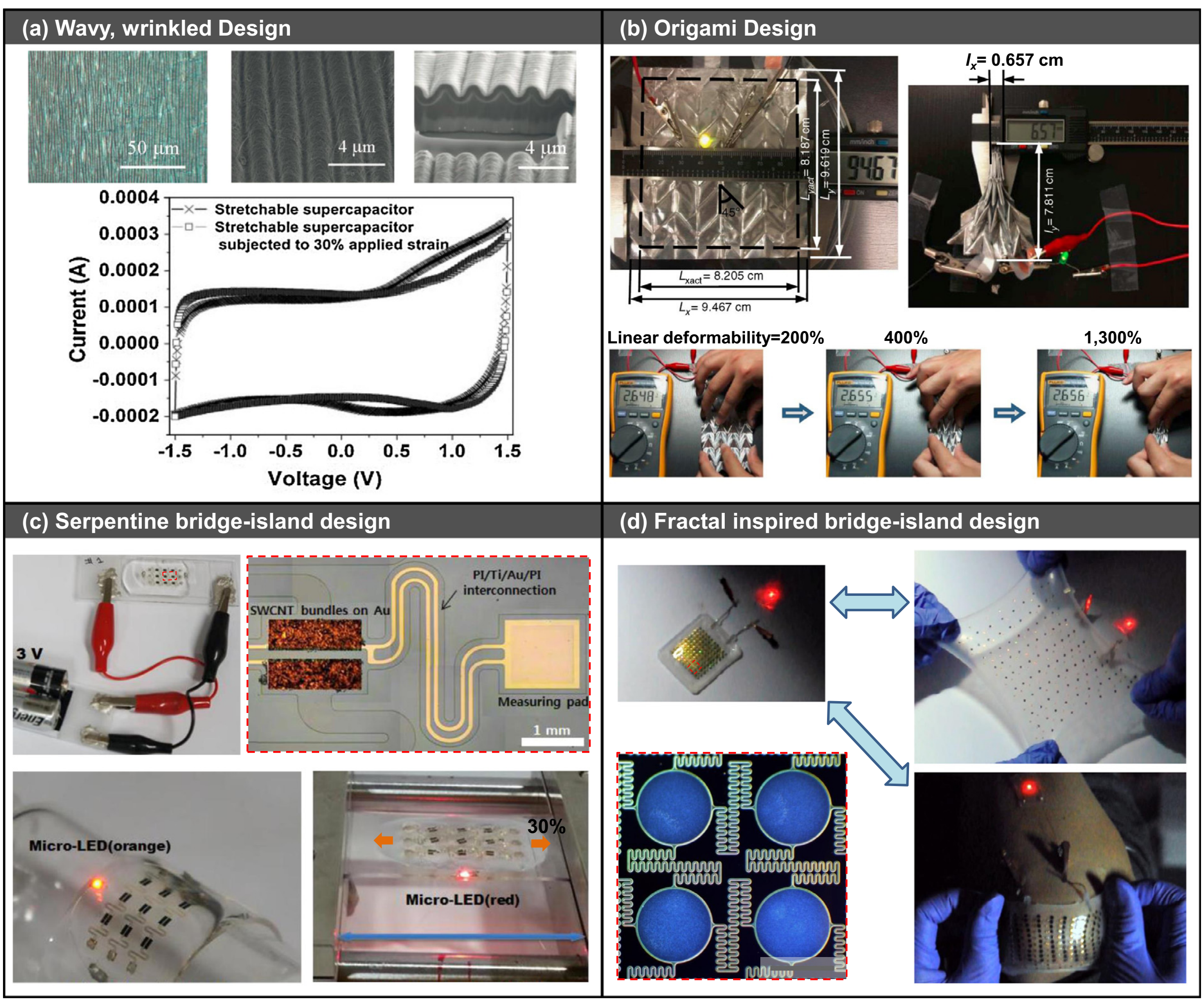

Fig. 1. Four representative mechanics-guided design strategies to enable stretchable batteries and/or supercapacitors. (a) Wavy, wrinkled design: optical microscopy and SEM images (top panels) of a 50-nm-thick, buckled SWNT macrofilm on a PDMS substrate with 30% prestrain, and cyclic voltammograms (bottom panel) of the stretchable supercapacitors under 0% and 30% unaxial strain, along with traditional supercapacitors using the pristine SWNT film for comparison. (b) Origami design: photographs (top panels) of the origami batteries operating a light-emitting diodes (LED), in the completely unfolded and compressed states, and the images (bottom panels) of linear deformation of an origami battery connected to a voltmeter. (c) Serpentine bridge-island design: photographs of stretchable supercapacitors under the charging state at 3 V (left top panel) and discharging state lighting a LED under bent (with a bending radius of ~2.5 cm, left bottom panel) and 30% stretched state (right bottom panel), and optical microscope image (right top panel) of an individual micro-supercapacitor with serpentine interconnections. (d) Fractal inspired bridge-island design: operation of a battery connected to a red LED, while undeformed (left top panel), biaxially stretched to 300% (right top panel), and mounted on the human elbow (right bottom panel), and optical image (scale bar, 2 mm) of the Al electrode pads and self-similar interconnects (left bottom panel). (a) is adapted with permission from Ref. [14], Copyright 2009, WILEY-VCH Verlag GmbH & Co. KGaA, Weinheim. (b) and (d) are adapted with permission from Refs. [27] (Copyright 2014) and [30] (Copyright 2013), Nature Publishing Group. (c) is adapted from with permission from Ref. [28], Copyright 2013, American Chemical Society.

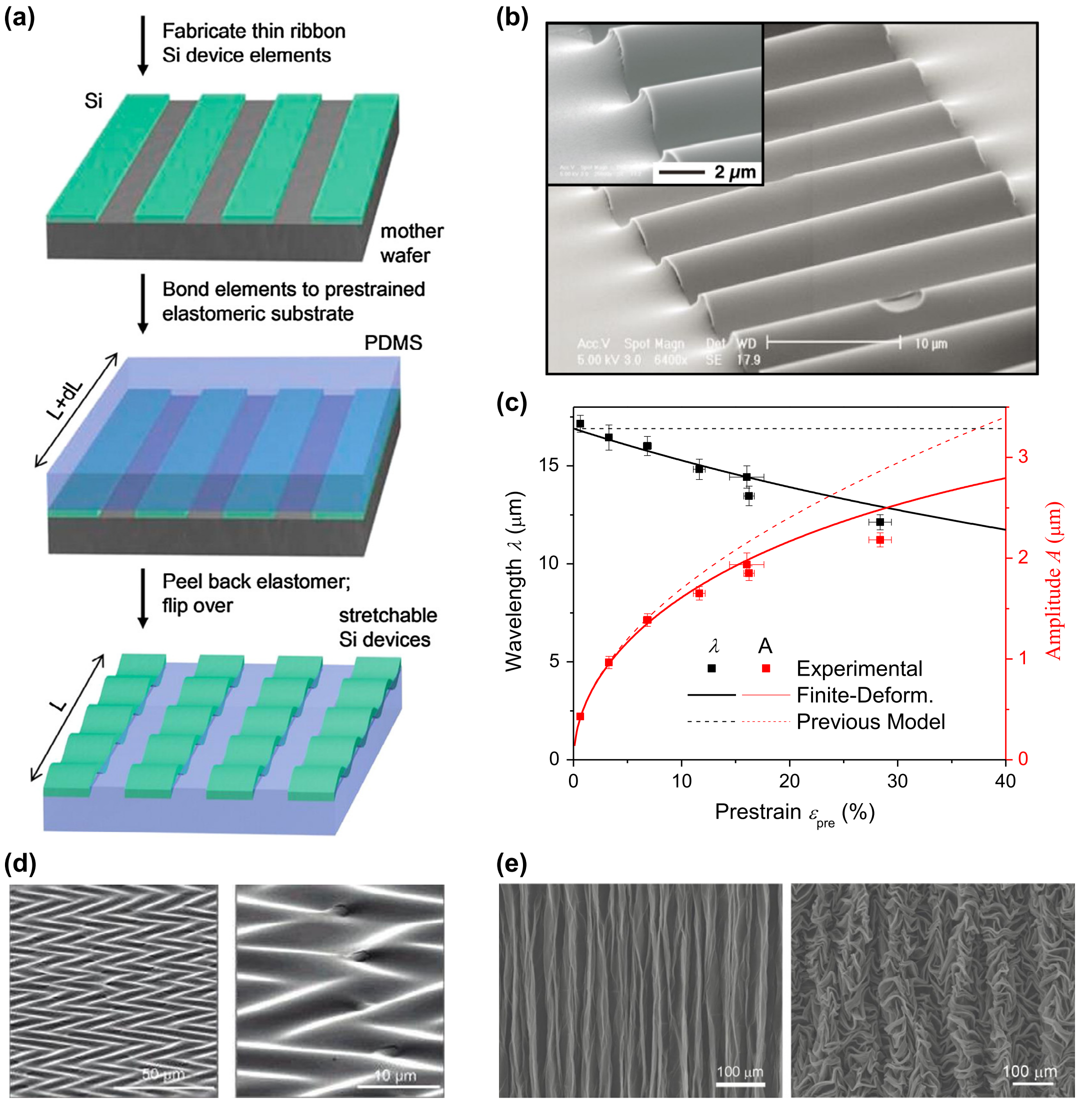

Fig. 2. (a) Schematic illustration of the process for fabricating wavy, wrinkled single crystal Si ribbons on an elastomeric substrate. (b) SEM images of wavy, wrinkled, single-crystal Si ribbons fabricated with a substrate prestrain of ~15%. (c) Dependences of wavelength and amplitude on the prestrain for wrinkled structures of Si (100 nm thickness) on PDMS. (d) SEM images of a 2D wavy Si nanomembrane fully bonded on PDMS. (e) Parallel ridges (left panel) and crumpled patterns (right panel) of graphene papers as the biaxially prestretched (~400%) elastomeric substrate is uniaxially and biaxially relaxed, respectively. (a) is adapted with permission from Ref. [34], Copyright 2006, American Association for the Advancement of Science. (b) and (c) are adapted with permission from Ref. [35], Copyright 2007, National Academy of Sciences. (d) is adapted with permission from Ref. [43], Copyright 2007, American Chemical Society. (e) is adapted with permission from Ref. [25], Copyright 2014, Nature Publishing Group.

semi-infinite solid. In this approach, a sinusoidal out-of-plane displacement is assumed for the bucked thin ribbon, with the wavelength (λ_0) and amplitude (A_0) that are determined through the minimization of total strain energy (in both the ribbons and substrate), as given by

$$\lambda_0 = \frac{\pi h_f}{\sqrt{\varepsilon_c}} = 2\pi h_f \left(\frac{\bar{E}_f}{3\bar{E}_s}\right)^{1/3}, \qquad A_0 = h_f\sqrt{\frac{\varepsilon_{\rm pre}}{\varepsilon_c} - 1}, \tag{1}$$

where the subscripts 'f' and 's' denote the ribbon and substrate, respectively; h_f is the ribbon thickness; $\bar{E} = E/(1-\nu^2)$ is the plane-strain modulus, with ν denoting the Poisson ratio; $\varepsilon_{\rm pre}$ is the prestrain of substrate; and $\varepsilon_c = (3\bar{E}_s/\bar{E}_f)^{2/3}/4$ is the critical or minimum strain that is necessary for buckling to occur, which is calculated as 0.034% for the Si ribbon (E_f = 130 GPa, υ_f = 0.27) on a PDMS substrate (E_f = 1.8 MPa, υ_f = 0.48). Since the membrane strain is usually much smaller than the bending strain, the peak strain in the buckled ribbon can be approximated as $\varepsilon_{\rm peak} \approx 2\sqrt{\varepsilon_{\rm pre}\varepsilon_c}$, from which the maximum prestrain can be determined to avoid fracture in the ribbons. Eq. (1) indicates a constant wavelength independent on the prestrain (corresponding to previous model in Fig. 2c), and agrees reasonably well with experimental measurements only when the prestrain is rather small (e.g., <5%).

In the regime of large prestrain (e.g., 5% < $\varepsilon_{\rm pre}$ < 30%), the experimental observations show a reduced wavelength with increasing prestrain, which can be mainly attributed to the finite deformation in the compliant substrate [35]. Jiang et al. [35] and Song et al. [40] developed analytic models to account for such effect, which, in particular, involves the difference of initial strain-free configurations for the substrate and films, the nonlinear strain–displacement relation in the substrate (and film), and the nonlinear stress–strain relation in the substrate. Based on minimization of total strain energy in this theoretical framework, the buckling wavelength and amplitude can be derived as

$$\lambda = \frac{\lambda_0}{(1+\varepsilon_{\rm pre})(1+\xi)^{1/3}}, \qquad A = \frac{A_0}{\sqrt{1+\varepsilon_{\rm pre}}(1+\xi)^{1/3}}, \tag{2}$$

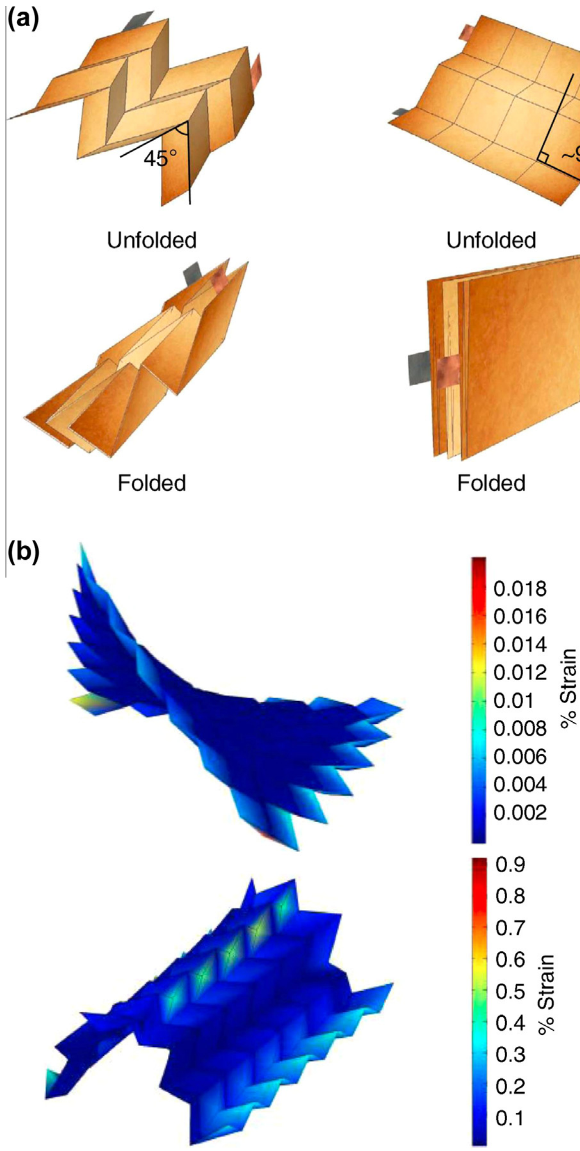

Fig. 3. (a) Schematic illustration of two representative origami patterns using Miura folding. (b) FEA results of a 45° Miura pattern under twisting (with ~90° twisting angle per unit cell) (top panel), and bending (with a bending radius of two unit cells) (bottom panel). Adapted with permission from Ref. [27], Copyright 2014, Nature Publishing Group.

where λ_0 and A_0 correspond to the wavelength and amplitude in the small-strain condition (in Eq. (1)), and $\xi = 5\varepsilon_{\mathrm{pre}}(1+\varepsilon_{\mathrm{pre}})/32$. Fig. 2c shows that the new solutions (Eq. (2)) could well capture the phenomenon of strain-dependent wavelength with a good accuracy, and reduce the difference between amplitude predictions and experimental results as compared to small-deformation solutions. The peak strain in this regime can be approximated by $\varepsilon_{\mathrm{peak}} \approx 2\sqrt{\varepsilon_{\mathrm{pre}}\varepsilon_c}(1+\xi)^{1/3}/\sqrt{1+\varepsilon_{\mathrm{pre}}}$, which give a maximum prestrain of ~29% for Si with a fracture strain of ~1.8%, and therefore indicates the stretchability of the wavy Si ribbons to be as large as ~29%. By extending this energy approach, Jiang et al. [41] and Cheng et al. [42] developed analytic models to study the effects of finite ribbon width and bi-layer substrate.

The above mechanical strategy was further extended by Choi et al. [43] and Kim et al. [44] to generate two-dimensional (2D), wavy, electronic devices (as shown in Fig. 2d), which could provide stretchability along all in-plane directions. Several computational and theoretical studies of the buckling configurations have been carried out in the case of biaxial prestrain [38,39,45,46]. Zang et al. [25,47] further introduced this design concept in graphene films (with 3–10 layers) on elastomeric substrate, in which extremely large prestrains (e.g., up to 400%) can be adopted to form ridged or crumpled patterns of graphene films (as shown in Fig. 2e).

3. Origami design

The introduction of origami design into stretchable batteries was recently demonstrated by Cheng et al. [26] and Song et al. [27] to achieve high areal energy density and unprecedented deformability, with an example shown in Fig. 1b. Origami is an ancient art of paper folding, in which the key is to form strategically designed creases. Two representative examples are shown in Fig. 3a through the Miura folding [27], in which many identical parallelogram faces are connected by 'mountain' and 'valley' creases. By adopting different angles between adjacent 'mountain' and 'valley' creases, the Miura-origami can be either completely compressible along one direction (left panel of Fig. 3a, which can be referred to as '45° Miura folding') or collapsible in two directions (right panel of Fig. 3a, which can be referred to as '90° Miura folding'). The representative unit cell of 45° Miura-origami consists of four identical parallelograms [48,49], with the short sides of length a, the long sides of length b, and the acute angle $\beta \propto [0°, 90°]$. Once the shape of parallelograms is prescribed, only one geometric parameter (i.e., the projection angle between two ridges, $\phi \propto [0°, 2\beta]$) is required to characterize the folding of Miura-origami, with $\phi = 2\beta$ and $\phi = 0°$ representing the planar state and completely collapsed state, respectively.

Under external mechanical loadings, the parallelogram faces themselves usually remain undeformed since the folding and unfolding of the creases maintains the faces in a rigid configuration. Therefore, the deformability at the system level is prescribed by the creases, while the base or constituent materials making the origami pattern do not experience large strain except at the creases. In this sense, the curvature radius of the creases becomes critical in the origami design to reduce the strain level for avoiding fracture or plastic yielding. Due to the complex geometry of origami design, only the effective mechanical properties, e.g., bending rigidity and Poisson ratio, were studied through analytic modeling [48,49], while the detailed deformation and strain distribution were examined mainly through computational studies based on finite element analyses (FEA) [27]. Fig. 3b shows an example of deformation and strain distributions in 45° Miura-origami under twisting and bending, in which the small level of maximum principal strain (<0.9%) illustrates the key mechanics advantage [27].

4. Serpentine bridge-island design

The bridge-island design with lithographically defined, filamentary, serpentine interconnects represents another strategy used to achieve stretchable supercapacitors, with an example shown in Fig. 1c that consists of planar SWCNT electrodes and an ionic liquid-based triblock copolymer electrolyte [28,29]. This design was initially introduced by Kim et al. [50], in which the functional components reside on the island, while the serpentine interconnects form the bridge. Under stretching, the serpentine interconnects (which have low effective stiffness) deform to provide the stretchability, while the rigid islands (which have high effective stiffness) keep almost undeformed (e.g., with <1% strain) to ensure the mechanical integrity of functional materials. Fig. 4a presents a schematic illustration of a serpentine interconnect with m unit cells, in which the representative unit cell consists of two half circles that are connected by straight lines, with the height h and spacing l. Based on different structural designs and fabrication processes,

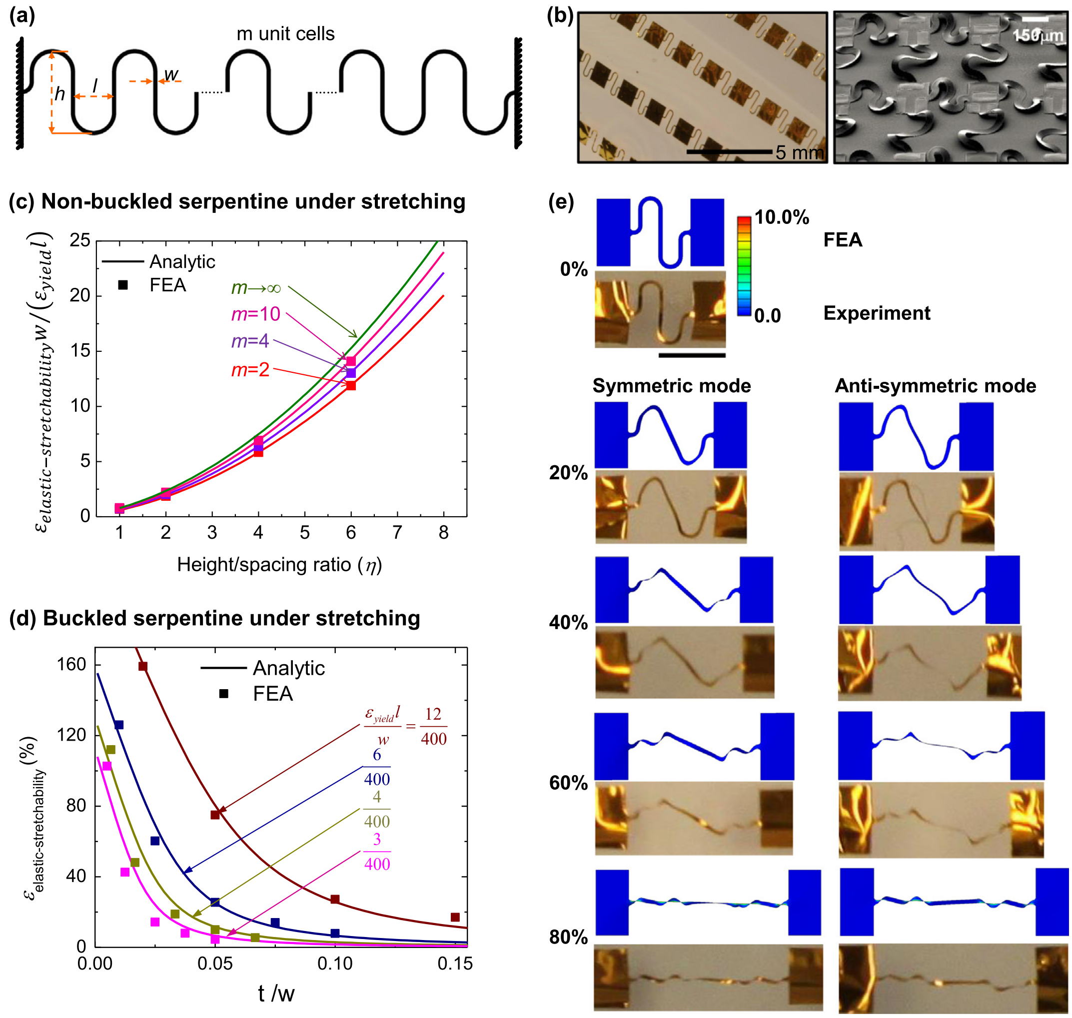

Fig. 4. (a) Schematic illustration of geometric parameters for a representative serpentine interconnect with m unit cells. (b) Optical image (left panel) of a coplanar serpentine bridge-island structure and SEM image (right panel) of a non-coplanar serpentine bridge-island structure enable by substrate prestrain. (c) Normalized elastic-stretchability of non-buckled, thick, serpentine interconnect as a function of height/spacing aspect ratio for different number of unit cells. (d) Elastic-stretchability of buckled, thin, serpentine interconnect as a function of thickness/width aspect ratio for various $\varepsilon_{\text{yield}}l/w$, $m = 1$ and $\eta = 4$. (e) Optical images and corresponding FEA predictions on buckling deformation of thin serpentine interconnects with symmetric (left panel) and anti-symmetric (right panel) modes. (a), (d) and (e) are adapted from with permission from Ref. [51], Copyright 2013, Royal Society of Chemistry. (b) is adapted from with permission from Refs. [51] (Copyright 2013, Royal Society of Chemistry) and [50] (Copyright 2008, National Academy of Sciences). (c) is adapted from with permission from Ref. [52], Copyright 2013, Elsevier Science Ltd.

the serpentine interconnect can be fully bonded, partially bonded, or completely non-bonded to the elastomeric substrate, each with different advantages/disadvantages for various application requirements. The underlying mechanics of serpentine interconnect is highly dependent on the bonding conditions, as detailed below.

The completely non-bonded serpentine interconnects are usually clamped at two ends by the rigid islands (in left panel of Fig. 4b) that are fully bonded to the substrates or raised surface relief structures from the substrates [51]. Non-coplanar configurations of the serpentine interconnect can be realized by using prestrain of substrate [50], as shown in the right panel of Fig. 4b. When the non-bonded serpentine interconnects are stretched from two ends, two different deformation modes could occur depending on the thickness/width ratio (t/w) [51]: (i) non-buckled, in-plane deformations, for large t/w (typically comparable to or larger than 1); (ii) buckled deformations that involve not only in-plane but also out-of-plane deformations, for small t/w (typically smaller than 1/5). The occurrence of buckling can be accurately determined by comparing the applied strain to critical buckling strain that can be expressed analytically in terms of the geometrical parameters [51]. The critical buckling strain increases, in a proportional manner, with the square of thickness/width ratio (t^2/w^2), indicating that buckling is much easier to occur in thinner serpentine interconnects.

For non-buckled serpentine interconnects under stretching, the beam theory can be adopted to solve the elastic stretchability as [52]

$$\varepsilon_{\text{elastic-stretchability}} = \frac{2\varepsilon_{\text{yield}}l}{mw}\frac{\bar{T}_{11}\bar{T}_{22}\bar{T}_{33} - \bar{T}_{11}(\bar{T}_{23})^2 - \bar{T}_{33}(\bar{T}_{12})^2}{2\bar{T}_{12}\bar{T}_{23} - 3\bar{T}_{12}\bar{T}_{33} + [\bar{T}_{22}\bar{T}_{33} - (\bar{T}_{23})^2](\eta - 1) + \sqrt{[\bar{T}_{22}\bar{T}_{33} - (\bar{T}_{23})^2]^2 + (\bar{T}_{12})^2(\bar{T}_{33})^2}}, \tag{3}$$

where η is the height/spacing aspect ratio (h/l), $\varepsilon_{\text{yield}}$ is the yield strain of interconnect material (e.g., 0.3% for copper), and $\bar{T}_{ij}$ ($i,j = 1,\ldots,3$) denotes the component of dimensionless flexibility matrix that measures the force–displacement relationship [52], as given by

$$\bar{T} = \frac{m}{24}\begin{Bmatrix} 4(\eta-1)^3 + 6\pi(\eta-1)^2 + 24(\eta-1) + 3\pi & 6[(\eta-1)^2 + \pi(\eta-1) + 2] & 0 \\ 6[(\eta-1)^2 + \pi(\eta-1) + 2] & 32m^2[2(\eta-1)+\pi] + 8(\eta-1) + \pi & 48m(\eta-1+\pi) \\ 0 & 48m(\eta-1+\pi) & 24(2\eta-2+\pi) \end{Bmatrix}, \tag{4}$$

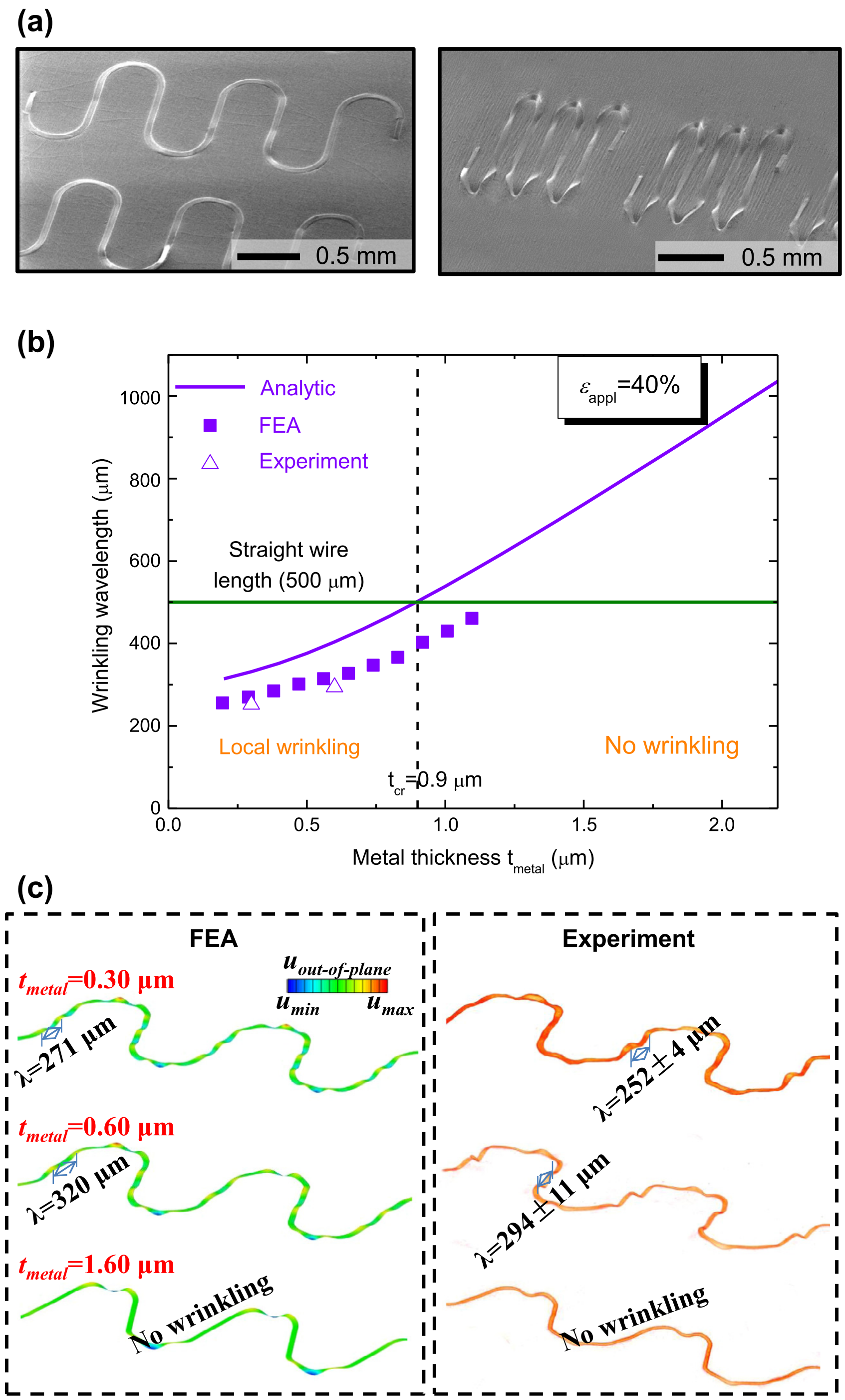

Fig. 5. (a) SEM images of serpentine interconnects fully bonded onto elastomeric substrate with (left panel) and without (right panel) use of prestrain. (b) Wrinkling wavelength as a function of the metal thickness, based on experiment, FEA and analytic modeling. (c) FEA results (left panel) and 3D MicroXCT scanning images (right panel) of the deformed configurations for three typical metal thicknesses to illustrate the two different buckling modes. The color of FEA results in (c) represents the distribution of out-of-plane displacement. The metal interconnects are sandwiched by two polyimide layers (1.2 μm), and mounted on a soft (60 kPa) substrate (0.5 mm). Adapted with permission from Ref. [57], Copyright 2014, WILEY-VCH Verlag GmbH & Co. KGaA, Weinheim.

where the membrane energy is neglected. The normalized stretchability $\varepsilon_{\text{elastic-stretchability}} w/(\varepsilon_{\text{yield}} l)$ increases with both the height/spacing ratio η and number of unit cell m, as shown in Fig. 4c, and saturates to

$$\frac{\varepsilon_{\text{elastic-stretchability}} w}{\varepsilon_{\text{yield}} l} = \frac{4\eta^3 + 6(\pi-2)\eta^2 - 12(\pi-3)\eta + 9\pi - 28}{12\eta} \quad (5)$$

for $m \to \infty$ (also shown in Fig. 4c). Widlund et al. [53] derived a different solution of stretchability for non-buckled serpentine structures, based on the 2D elasticity theory, which could provide a more accurate prediction, in particular for relative large width/spacing ratio (w/l) and small height/spacing ratio (η).

For buckled serpentine interconnects under stretching, Zhang et al. [51] obtained a semi-analytic solution of elastic stretchability as

$$\varepsilon_{\text{elastic-stretchability}} = \chi^2, \quad (6)$$

where $\chi > 0$ is the solution of the following 4th order algebraic equation that has a single positive solution,

$$g_2(m,\eta)\chi^4 + g_1(m,\eta)\frac{t}{w}\chi - \frac{\varepsilon_{\text{yield}} l}{w} = 0, \quad (7)$$

where g_1 and g_2 depend on the number of unit cell m and height/spacing ratio η, and are determined by FEA [51]. Fig. 4d shows that the predictions of this semi-analytic solution agree well with the numerical results for a large range of t/w and $\varepsilon_{\text{yield}} l/w$, with both indicating that the elastic stretchability increases with decreasing serpentine thickness (via t/w) or increasing spacing or yield strain (via $\varepsilon_{\text{yield}} l/w$). The analytic modeling of the detailed buckling processes is quite challenging, which can be complemented by FEA [50,51,54]. Fig. 4e illustrates the evolution of deformations associated with two different buckling modes for strains between 0% to 80%, in which remarkable agreements can be observed between FEA and experimental results [51]. It is noteworthy that the geometric parameters of the serpentines place them at the transition region between two different buckling modes, such that both modes can occur.

The fully bonded serpentine interconnects also involve coplanar and non-coplanar configurations as shown in the left and right panels of Fig. 5a. The deformation modes of such fully bonded system become quite complicated as compared to completely non-bonded case, due to the constraints from substrate deformation. For this reason, the existing studies on the analyses of stretchability (and elastic stretchability) mainly relied on computational approaches based on 3D FEA [3,55–62]. Zhang et al. [57] studied systematically the effects of key geometric and materials parameters on the elastic stretchability and the enhancements enabled by the prestrain strategy. The FEA calculations indicate a drastic decrease in the elastic stretchability with increasing metal thickness, which can be mainly attributed to changes in the buckling mode, i.e., from local wrinkling at small thicknesses to absence of such wrinkling at large thicknesses, as revealed by experiment in Fig. 5c. The associated mechanics results from a competition between the buckling wavelength and the length of the straight segments of the serpentine structure, as illustrated in Fig. 5b, through combined analytic, FEA and experiment results.

5. Fractal inspired bridge-island design

The fractal inspired interconnect designs could make full use of a limited space by increasing the fractal order, thereby with a great advantage in enhancing, simultaneously, the areal energy density and system stretchability of batteries, as illustrated by Xu et al. [30] in an ultra-stretchable lithium-ion battery (shown by Fig. 1d). Here, the key is to design an appropriate fractal layouts of the interconnects that could fit well with the other components of the battery. Fig. 6a provides an example of fractal layout (with fractal order n up to 4) starting with the serpentine configuration as the 1st order structure. The nth order serpentine interconnect is created by reducing the scale of the $(n-1)$th order interconnect,

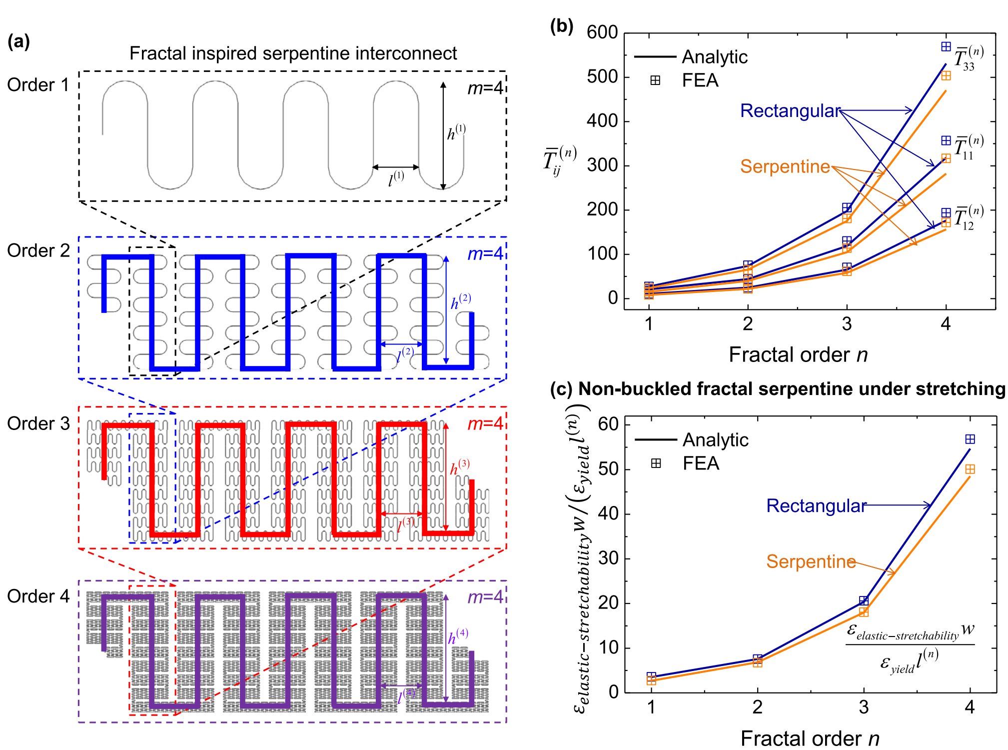

Fig. 6. (a) Geometric construction of fractal inspired serpentine interconnects from order 1 to 4. (b) Three representative normalized flexibility components versus the fractal order. (c) Normalized elastic-stretchability of non-buckled, thick, fractal serpentine interconnect versus the fractal order. The width is fixed as $w = 0.4l^{(1)}$ for the structures of different orders in the FEA results shown in (b) and (c). Adapted with permission from Ref. [52], Copyright 2013, Elsevier Science Ltd.

followed by 90° rotation, and then connecting multiple copies of them in a fashion to reproduce the layout of original geometry. According to the self-similar nature in geometry [63], the length parameters [spacing $l^{(i)}$, height $h^{(i)}$] at any order can be scaled with the spacing of the highest order $l^{(n)}$ by

$$l^{(i)} = \left[\prod_{k=1}^{n-i} \frac{\eta^{(n-k+1)}}{2m^{(n-k)}}\right] l^{(n)}, \qquad h^{(i)} = \eta^{(i)} \left[\prod_{k=1}^{n-i} \frac{\eta^{(n-k+1)}}{2m^{(n-k)}}\right] l^{(n)}, \quad (i = 1, \ldots, n-1), \tag{8}$$

where $m^{(i)}$ and $\eta^{(i)} = h^{(i)}/l^{(i)}$ are the number of unit cells and height/spacing aspect ratio at order i. To keep the overall geometry exactly the same at each order, these two parameters should be all the same at each order, which, however, may not be necessary in practical applications.

Similar to the serpentine interconnects, the fractal inspired interconnects (simply referred to as fractal interconnects) can be also made fully bonded, or completely non-bonded to the elastomeric substrate. Stretched from two ends, the non-bonded fractal interconnects also undergo non-buckled, in-plane deformations for large t/w (typically comparable to or larger than 1), and buckled deformations for small t/w (typically smaller than 1/5). For non-buckled fractal rectangular and serpentine interconnects under stretching, Zhang et al. [52] developed analytical models of flexibility and elastic stretchability, through establishing the recursive formulae at different fractal orders. Fig. 6b illustrates that the analytic flexibility components, as validated by FEA results, all increase with fractal order (n), and are more than doubled for each n increasing by 1. The analytic solution of elastic stretchability is also in good agreement with FEA results, as shown in Fig. 6c, with both indicating that the elastic limit of the interconnect can be well improved by adopting higher order fractal design.

For buckled fractal serpentine interconnects under stretching, an interesting deformation mechanism of ordered unraveling was unveiled by Xu et al. [30], through combined mechanics modeling and experiment measurement. As shown in Fig. 7a, the 2nd order structure (i.e., the large spring) unravels first via out-of-plane bending and twisting through buckling, during which there is essentially no deformation in the 1st order structure (i.e., the small spring) (see top 4 images in Fig. 7a). The unraveling of the 1st order structure only starts as the 2nd order structure is fully extended (corresponding to an applied strain of ~150%), and continues until the stretchability (~300%) is reached (see bottom 3 images in Fig. 7a). Based on this unique mechanism, Zhang et al. [63] developed an effective and robust hierarchical computational model (HCM), for postbuckling analysis of the fractal interconnects, which could reduce substantially the computational efforts and costs as compared to conventional FEA. Fig. 7a–c illustrate that this HCM has a good accuracy in predictions of the deformation and strain magnitude for the fractal serpentine interconnects [63]. The results in Fig. 7c show that the elastic stretchability increases by >3 times for each increase of n by 1, which represents a huge increase (~200 times) of elastic stretchability from ~10.7% for the 1st order, to ~2140% for the 4th order.

For fully bonded fractal interconnects, Fan et al. [64] studied the deformations of various deterministic fractal layouts, including Peano, Greek cross, Hilbert, Vicsek and other space-filling curves, as shown in Fig. 8. The FEA predictions of deformed configurations (Fig. 8b) agree well with the experimental images (Fig. 8c) for all the different fractal layouts. A high precision electro-mechanical

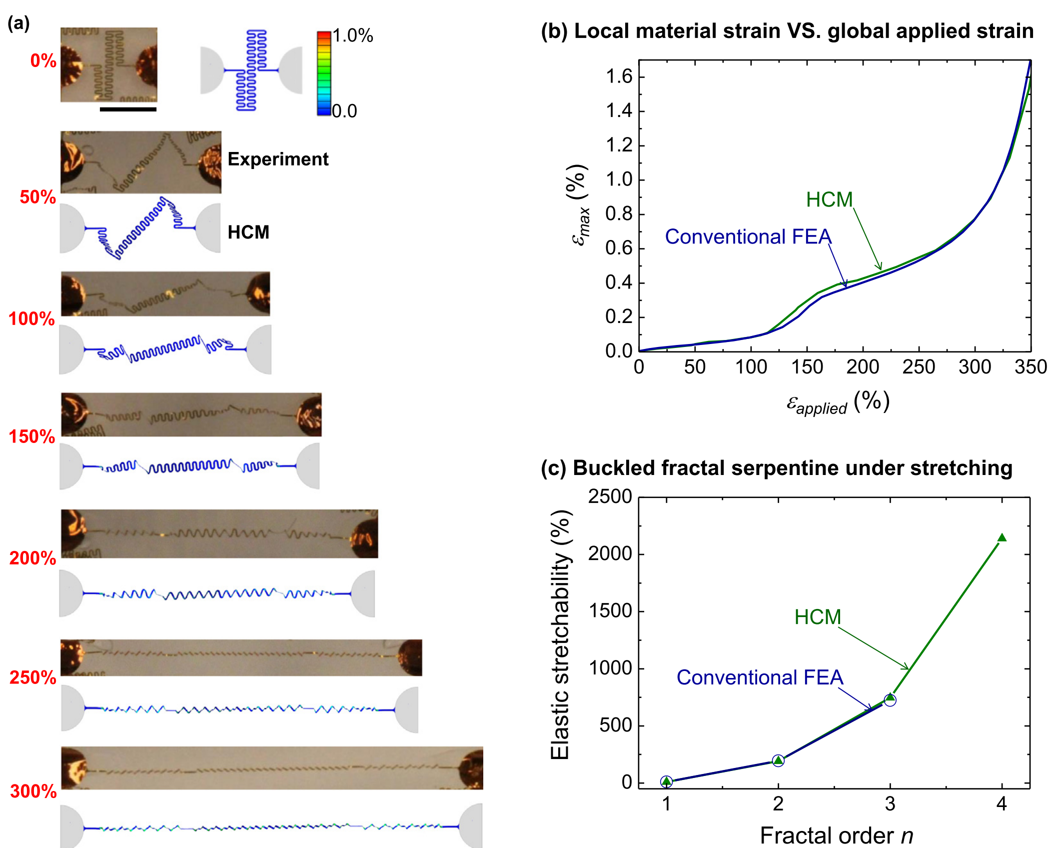

Fig. 7. (a) Optical images and corresponding predictions based on HCM for a 2nd order fractal interconnect under various stages of stretching. (b) Maximum principal strain of material versus the applied strain for 2nd order fractal interconnects in (a), based on calculations of HCM and conventional FEA. (c) Elastic-stretchability versus the fractal order for buckled, thin, fractal serpentine interconnect from n = 1–4, with $(m, \eta) = (4, 8/\sqrt{11})$, the thickness/width aspect ratio (t/w = 0.03), and the width to spacing ratio ($w/l^{(1)} = 0.4$), for structures of different fractal orders. The color in HCM results shown in (a) represents the magnitude of maximum principal strain. Adapted from permission from Refs. [30] (Copyright 2013, Nature Publishing Group) and [63] (Copyright 2014, Elsevier Science Ltd).

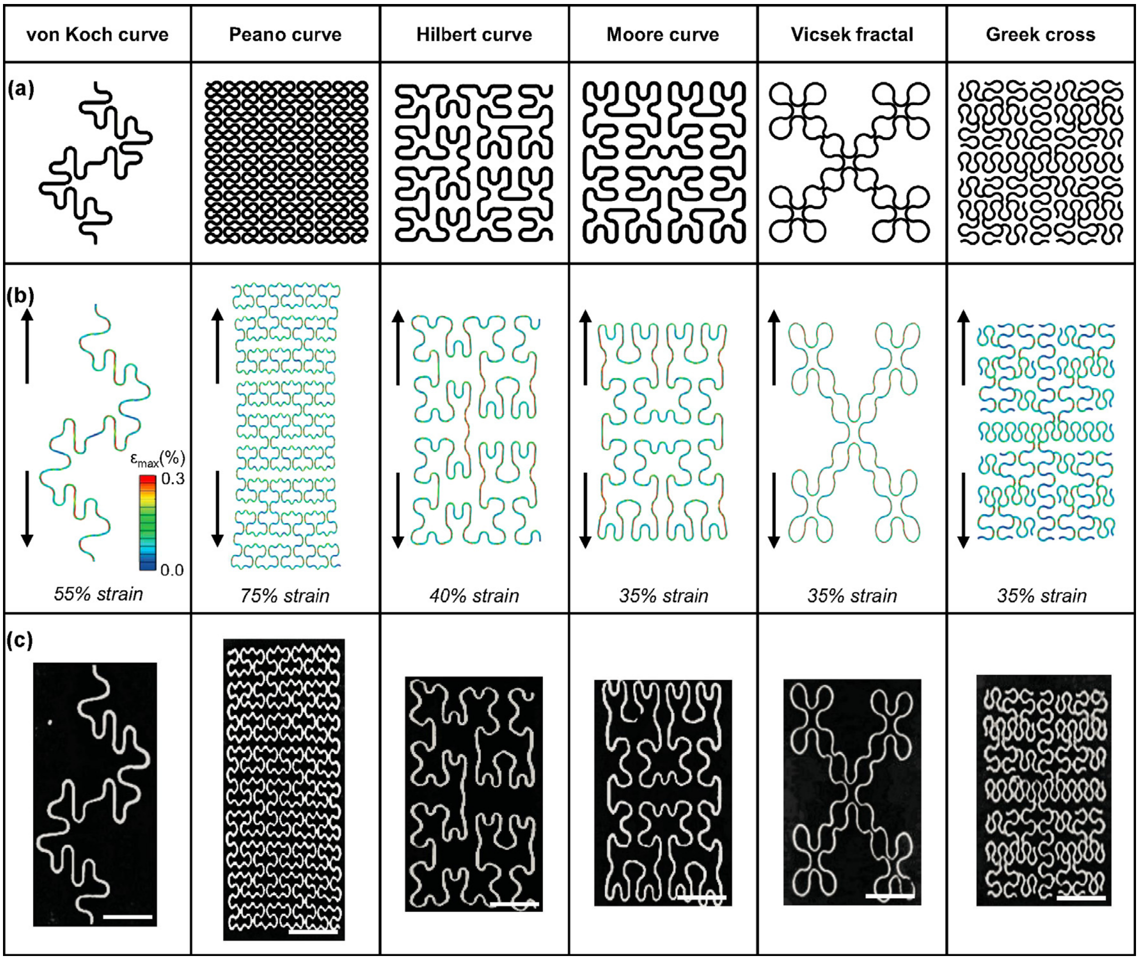

Fig. 8. (a) Fractal inspired interconnects with six different topologies, which are fully bonded onto elastomeric substrates. (b) FEA calculations and (c) corresponding experimental MicroXCT images (scale bars, 2 mm) of each structure under elastic tensile strain. The interconnects consist of a gold layer (300 nm) sandwiched by two polyimide layers (1.2 μm), and are mounted on a soft (50 kPa) substrate (0.5 mm). Adapted from permission from Ref. [64], Copyright 2014, Nature Publishing Group.

approach was also introduced by Fan et al. [64] to measure the elastic–plastic transition (or the elastic stretchability) for the fractal interconnects, which shows reasonable accordance with FEA calculations. Due to the mechanical constraints of the elastomeric substrate, the elastic stretchability of fully bonded fractal interconnects is usually much lower than the counterpart of completely non-bonded interconnects [5].

6. Concluding remarks

Fast developments and substantial achievements have been made on various aspects of stretchable energy storage systems, driven mainly by advances in the field of stretchable electronics that have already yielded sophisticated system-level demonstrators in important areas of application that cannot be addressed with any other approach. The designs rely critically on extreme forms of mechanics-guided heterogeneous integration of ultrahard (e.g., moduli approaching 1 TPa, for SWNTs and graphene [14,25]) and ultrasoft components (e.g., modulus ~3 kPa for certain cellular forms of elastomers [65], and ~60 kPa for ecoflex [30]), with four representative strategies reviewed in this paper. Quantitative mechanics design has been playing crucial roles, at a level of importance that is comparable to circuit design in conventional electronics [66]. While several efforts have been devoted to develop analytical and computational models for each specific strategy, most of these models were built with certain idealizations/assumptions, and may not be applicable for some extreme conditions that are also important for new emerging applications. As such, there are still many open challenges and opportunities for future research. For example, the complex morphology and failure of ridged (or crumpled) pattern [25,47,67] formed with a relative large uniaxial (or biaxial) strain (e.g., >200%), as shown in Fig. 2e, cannot be well predicted by the existing models. A theoretical mechanics model of the origami design [27] remains necessary to correlate the maximum material strain with the constructing geometric parameters under bending or twisting deformations. Besides, developing analytical and/or computational models that account for the interfacial delamination are also desirable for serpentine and fractal interconnects bonded onto or encapsulated in a soft elastomer. The topology optimization of interconnect configurations to identify a best layout for prescribed loading conditions remains as a virgin area of research.

Acknowledgements

J.A.R. acknowledges the support from NSF (DMR-1242240). Y.H. acknowledge the support from NSF (DMR-1121262 and CMMI-1400169), and from ISEN at Northwestern University.

References

[1] Rogers JA, Someya T, Huang YG. Materials and mechanics for stretchable electronics. Science 2010;327:1603–7.
[2] Sekitani T, Someya T. Stretchable, large-area organic electronics. Adv Mater 2010;22:2228–46.

[3] Kim DH, Lu NS, Ma R, Kim YS, Kim RH, Wang SD, et al. Epidermal electronics. Science 2011;333:838–43.
[4] Kaltenbrunner M, Sekitani T, Reeder J, Yokota T, Kuribara K, Tokuhara T, et al. An ultra-lightweight design for imperceptible plastic electronics. Nature 2013;499:458–63.
[5] Xu S, Zhang YH, Jia L, Mathewson KE, Jang KI, Kim J, et al. Soft microfluidic assemblies of sensors, circuits, and radios for the skin. Science 2014;344:70–4.
[6] Ko HC, Stoykovich MP, Song JZ, Malyarchuk V, Choi WM, Yu CJ, et al. A hemispherical electronic eye camera based on compressible silicon optoelectronics. Nature 2008;454:748–53.
[7] Song YM, Xie YZ, Malyarchuk V, Xiao JL, Jung I, Choi KJ, et al. Digital cameras with designs inspired by the arthropod eye. Nature 2013;497:95–9.
[8] Yu Z, Graudejus O, Tsay C, Lacour SP, Wagner S, Morrison B. Monitoring hippocampus electrical activity in vitro on an elastically deformable microelectrode array. J Neurotrauma 2009;26:1135–45.
[9] Graudejus O, Morrison B, Goletiani C, Yu Z, Wagner S. Encapsulating elastically stretchable neural interfaces: yield, resolution, and recording/stimulation of neural activity. Adv Funct Mater 2012;22:640–51.
[10] Kim DH, Wang SD, Keum H, Ghaffari R, Kim YS, Tao H, et al. Thin, flexible sensors and actuators as 'Instrumented' surgical sutures for targeted wound monitoring and therapy. Small 2012;8:3263–8.
[11] Lacour SP, Jones J, Suo Z, Wagner S. Design and performance of thin metal film interconnects for skin-like electronic circuits. IEEE Electron Device Lett 2004;25:179–81.
[12] Someya T, Sekitani T, Iba S, Kato Y, Kawaguchi H, Sakurai T. A large-area, flexible pressure sensor matrix with organic field-effect transistors for artificial skin applications. PNAS 2004;101:9966–70.
[13] Benight SJ, Wang C, Tok JBH, Bao ZA. Stretchable and self-healing polymers and devices for electronic skin. Prog Polym Sci 2013;38:1961–77.
[14] Yu CJ, Masarapu C, Rong JP, Wei BQ, Jiang HQ. Stretchable supercapacitors based on buckled single-walled carbon nanotube macrofilms. Adv Mater 2009;21:4793–7.
[15] Hu LB, Pasta M, La Mantia F, Cui LF, Jeong S, Deshazer HD, et al. Stretchable, porous, and conductive energy textiles. Nano Lett 2010;10:708–14.
[16] Kaltenbrunner M, Kettlgruber G, Siket C, Schwodiauer R, Bauer S. Arrays of ultracompliant electrochemical dry gel cells for stretchable electronics. Adv Mater 2010;22:2065–7.
[17] Gaikwad AM, Zamarayeva AM, Rousseau J, Chu HW, Derin I, Steingart DA. Highly stretchable alkaline batteries based on an embedded conductive fabric. Adv Mater 2012;24:5071–6.
[18] Meng YN, Zhao Y, Hu CG, Cheng HH, Hu Y, Zhang ZP, et al. All-graphene core-sheath microfibers for all-solid-state, stretchable fibriform supercapacitors and wearable electronic textiles. Adv Mater 2013;25:2326–31.
[19] Kettlgruber G, Kaltenbrunner M, Siket CM, Moser R, Graz IM, Schwodiauer R, et al. Intrinsically stretchable and rechargeable batteries for self-powered stretchable electronics. J Mater Chem A 2013;1:5505–8.
[20] Yan CY, Wang X, Cui MQ, Wang JX, Kang WB, Foo CY, et al. Stretchable silver-zinc batteries based on embedded nanowire elastic conductors. Adv Eng Mater 2014;4:1301396.
[21] Wang CY, Zheng W, Yue ZL, Too CO, Wallace GG. Buckled, stretchable polypyrrole electrodes for battery applications. Adv Mater 2011;23:3580–4.
[22] Li X, Gu TL, Wei BQ. Dynamic and galvanic stability of stretchable supercapacitors. Nano Lett 2012;12:6366–71.
[23] Zhao C, Wang CY, Yue ZL, Shu KW, Wallace GG. Intrinsically stretchable supercapacitors composed of polypyrrole electrodes and highly stretchable gel electrolyte. ACS Appl Mat Interfaces 2013;5:9008–14.
[24] Chen T, Xue YH, Roy AK, Dai LM. Transparent and stretchable high-performance supercapacitors based on wrinkled graphene electrodes. ACS Nano 2014;8:1039–46.
[25] Zang JF, Cao CY, Feng YY, Liu J, Zhao XH. Stretchable and high-performance supercapacitors with crumpled graphene papers. Sci Rep 2014;4:6492.
[26] Cheng Q, Song ZM, Ma T, Smith BB, Tang R, Yu HY, et al. Folding paper-based lithium-ion batteries for higher areal energy densities. Nano Lett 2013;13:4969–74.
[27] Song ZM, Ma T, Tang R, Cheng Q, Wang X, Krishnaraju D, et al. Origami lithium-ion batteries. Nat Commun 2014;5:3140.
[28] Kim D, Shin G, Kang YJ, Kim W, Ha JS. Fabrication of a stretchable solid-state micro-supercapacitor array. ACS Nano 2013;7:7975–82.
[29] Kim D, Yun J, Lee G, Ha JS. Fabrication of high performance flexible microsupercapacitor arrays with hybrid electrodes of MWNT/V2O5 nanowires integrated with a SnO2 nanowire UV sensor. Nanoscale 2014;6:12034–41.
[30] Xu S, Zhang YH, Cho J, Lee J, Huang X, Jia L, et al. Stretchable batteries with self-similar serpentine interconnects and integrated wireless recharging systems. Nat Commun 2013;4:1543.
[31] Xie KY, Wei BQ. Materials and structures for stretchable energy storage and conversion devices. Adv Mater 2014;26:3592–617.
[32] Bowden N, Brittain S, Evans AG, Hutchinson JW, Whitesides GM. Spontaneous formation of ordered structures in thin films of metals supported on an elastomeric polymer. Nature 1998;393:146–9.
[33] Jones J, Lacour SP, Wagner S, Suo ZG. Stretchable wavy metal interconnects. J Vac Sci Technol, A 2004;22:1723–5.
[34] Khang DY, Jiang HQ, Huang Y, Rogers JA. A stretchable form of single-crystal silicon for high-performance electronics on rubber substrates. Science 2006;311:208–12.
[35] Jiang HQ, Khang DY, Song JZ, Sun YG, Huang YG, Rogers JA. Finite deformation mechanics in buckled thin films on compliant supports. PNAS 2007;104:15607–12.
[36] Khang DY, Rogers JA, Lee HH. Mechanical buckling: mechanics, metrology, and stretchable electronics. Adv Funct Mater 2009;19:1526–36.
[37] Song J, Jiang H, Huang Y, Rogers JA. Mechanics of stretchable inorganic electronic materials. J Vac Sci Technol, A 2009;27:1107–25.
[38] Huang ZY, Hong W, Suo Z. Nonlinear analyses of wrinkles in a film bonded to a compliant substrate. J Mech Phys Solids 2005;53:2101–18.
[39] Chen X, Hutchinson JW. Herringbone buckling patterns of compressed thin films on compliant substrates. J Appl Mech – Trans ASME 2004;71:597–603.
[40] Song J, Jiang H, Liu ZJ, Khang DY, Huang Y, Rogers JA, et al. Buckling of a stiff thin film on a compliant substrate in large deformation. Int J Solids Struct 2008;45:3107–21.
[41] Jiang HQ, Khang DY, Fei HY, Kim H, Huang YG, Xiao JL, et al. Finite width effect of thin-films buckling on compliant substrate: experimental and theoretical studies. J Mech Phys Solids 2008;56:2585–98.
[42] Cheng HY, Zhang YH, Hwang KC, Rogers JA, Huang YG. Buckling of a stiff thin film on a pre-strained bi-layer substrate. Int J Solids Struct 2014;51:3113–8.
[43] Choi WM, Song JZ, Khang DY, Jiang HQ, Huang YY, Rogers JA. Biaxially stretchable "Wavy" silicon nanomembranes. Nano Lett 2007;7:1655–63.
[44] Kim DH, Ahn JH, Choi WM, Kim HS, Kim TH, Song JZ, et al. Stretchable and foldable silicon integrated circuits. Science 2008;320:507–11.
[45] Huang R, Im SH. Dynamics of wrinkle growth and coarsening in stressed thin films. Phys Rev E 2006;74:026214.
[46] Song J, Jiang H, Choi WM, Khang DY, Huang Y, Rogers JA. An analytical study of two-dimensional buckling of thin films on compliant substrates. J Appl Phys 2008;103:014303.
[47] Zang JF, Ryu S, Pugno N, Wang QM, Tu Q, Buehler MJ, et al. Multifunctionality and control of the crumpling and unfolding of large-area graphene. Nat Mater 2013;12:321–5.
[48] Lv C, Krishnaraju D, Konjevod G, Yu HY, Jiang HQ. Origami based mechanical metamaterials. Sci Rep 2014;4:5979.
[49] Wei ZY, Guo ZV, Dudte L, Liang HY, Mahadevan L. Geometric mechanics of periodic pleated origami. Phys Rev Lett 2013;110:215501.
[50] Kim DH, Song JZ, Choi WM, Kim HS, Kim RH, Liu ZJ, et al. Materials and noncoplanar mesh designs for integrated circuits with linear elastic responses to extreme mechanical deformations. PNAS 2008;105:18675–80.
[51] Zhang YH, Xu S, Fu HR, Lee J, Su J, Hwang KC, et al. Buckling in serpentine microstructures and applications in elastomer-supported ultra-stretchable electronics with high areal coverage. Soft Matter 2013;9:8062–70.
[52] Zhang YH, Fu HR, Su YW, Xu S, Cheng HY, Fan JA, et al. Mechanics of ultra-stretchable self-similar serpentine interconnects. Acta Mater 2013;61:7816–27.
[53] Widlund T, Yang SX, Hsu YY, Lu NS. Stretchability and compliance of freestanding serpentine-shaped ribbons. Int J Solids Struct 2014;51:4026–37.
[54] Li T, Suo ZG, Lacour SP, Wagner S. Compliant thin film patterns of stiff materials as platforms for stretchable electronics. J Mater Res 2005;20:3274–7.
[55] Gonzalez M, Axisa F, Bulcke MV, Brosteaux D, Vandevelde B, Vanfleteren J. Design of metal interconnects for stretchable electronic circuits. Microelectron Reliab 2008;48:825–32.
[56] Hsu Y-Y, Gonzalez M, Bossuyt F, Axisa F, Vanfleteren J, De Wolf I. The effects of encapsulation on deformation behavior and failure mechanisms of stretchable interconnects. Thin Solid Films 2011;519:2225–34.
[57] Zhang YH, Wang SD, Li XT, Fan JA, Xu S, Song YM, et al. Experimental and theoretical studies of serpentine microstructures bonded to prestrained elastomers for stretchable electronics. Adv Funct Mater 2014;24:2028–37.
[58] Huang YA, Duan YQ, Ding YJ, Bu NB, Pan YQ, Lu NS, et al. Versatile, kinetically controlled, high precision electrohydrodynamic writing of micro/nanofibers. Sci Rep 2014;4:5949.
[59] Huang YA, Wang YZ, Xiao L, Liu HM, Dong WT, Yin ZP. Microfluidic serpentine antennas with designed mechanical tunability. Lab Chip 2014;14:4205–12.
[60] Lu NS, Lu C, Yang SX, Rogers J. Highly sensitive skin-mountable strain gauges based entirely on elastomers. Adv Funct Mater 2012;22:4044–50.
[61] Duan YQ, Huang YA, Yin ZP, Bu NB, Dong WT. Non-wrinkled, highly stretchable piezoelectric devices by electrohydrodynamic direct-writing. Nanoscale 2014;6:3289–95.
[62] Gao L, Zhang YH, Malyarchuk V, Jia L, Jang KI, Webb RC, et al. Epidermal photonic devices for quantitative imaging of temperature and thermal transport characteristics of the skin. Nat Commun 2014;5:4938.
[63] Zhang YH, Fu HR, Xu S, Fan JA, Hwang KC, Jiang JQ, et al. A hierarchical computational model for stretchable interconnects with fractal-inspired designs. J Mech Phys Solids 2014;72:115–30.
[64] Fan JA, Yeo WH, Su YW, Hattori Y, Lee W, Jung SY, et al. Fractal design concepts for stretchable electronics. Nat Commun 2014;5:3266.
[65] Jang KI, Han SY, Xu S, Mathewson KE, Zhang YH, Jeong JW, et al. Rugged and breathable forms of stretchable electronics with adherent composite substrates for transcutaneous monitoring. Nat Commun 2014;5:4779.
[66] Kim DH, Lu NS, Huang YG, Rogers JA. Materials for stretchable electronics in bioinspired and biointegrated devices. MRS Bull 2012;37:226–35.
[67] Cao CY, Chan HF, Zang JF, Leong KW, Zhao XH. Harnessing localized ridges for high-aspect-ratio hierarchical patterns with dynamic tunability and multifunctionality. Adv Mater 2014;26:1763–70.